Formation of a trivalent chromium conversion coating on AZ91D magnesium alloy

Jiantao Qi, Zonghao Ye, Ning Gong, Xuelian Qu, Dimitri Mercier, Jolanta Światowska, Peter Skeldon, Philippe Marcus

Formation of a trivalent chromium conversion coating on AZ91D magnesium alloy

Jiantao Qi [a,*], Zonghao Ye [a], Ning Gong [a], Xuelian Qu [a, b], Dimitri Mercier [c], Jolanta Światowska [c,*], Peter Skeldon [d,*], Philippe Marcus [c]

[a] College of New Energy, China University of Petroleum (East China), Qingdao, 266580, PR China
[b] Qingdao Institute of Bioenergy and Bioprocess Technology, Chinese Academy of Science, 266101, PR China
[c] PSL Research University, Chimie Paris Tech – CNRS, Institut De Recherche De Chimie Paris, Physical Chemistry of Surfaces Group, 11 Rue Pierre Et Marie Curie, 75005, Paris, France
[d] Corrosion and Protection Centre, The University of Manchester, Oxford Rd., Manchester, M13 9PL, United Kingdom

A B S T R A C T

Trivalent chromium conversion (TCC) coating formation on AZ91D magnesium alloy has been investigated using scanning electron microscopy, energy X-ray dispersive spectroscopy (EDS), X-ray photoelectron spectroscoy (XPS). The coating was formed in a commercial SurTec 650 bath. XPS showed that coatings contained mainly Cr, Zr, O, S and F species, which were assigned to hydrated Cr(III) ($Cr(OH)_3$/CrOOH), ZrO_2, $Cr_2(SO_4)_3$, and CrF_3, and lower amounts of Mg^{2+} and Al^{3+} species assigned to oxide, hydroxide and fluoride. The Cr/Zr atomic ratio was around 0.5. The coating was formed above both α matrix and β ($Mg_{17}Al_{12}$) grain boundary regions, and it was significantly thicker above the cathodic β phase. Raman spectroscopy evidenced the presence of Cr(VI) species, formed due to oxidation of Cr(III) by H_2O_2, particularly in the coating above the cathodic sites. Electrochemical impedance spectroscopy revealed that corrosion protection was provided mainly by the barrier layer at the base of the coating, which resulted in a reduction

keywords: Trivalent chromium Conversion coating Magnesium alloy Corrosion protection Surface pre-treatment

1. Introduction

Owing to their light weight, magnesium alloys are often considered as next-generation structural materials in transportation systems. However, the reactivity of magnesium (standard electrode potential -2.37 V vs. SHE) and the presence of cathodic second phases lead to the high corrosion sensitivity in aqueous and atmospheric environments [1–3]. Chemical conversion treatment is often an economic and efficient surface treatment to provide corrosion protection. For instance, Hu et al. [4] treated AZ91D alloys in stannate solution, forming a 5 μm-thick coating that protected against corrosion in 3.5 % NaCl solution. Phosphate-based conversion coatings have also been employed that result in an insoluble deposit of $Mg_3(PO_4)_2$ [5]. Zai et al. compared different deposition parameters and revealed that a coating formed at 80 °C and at a pH 3 offered the best corrosion resistance [6]. Chunyan et al. [7] proposed a phosphate-based conversion coating using the ratio of total acidity (TA) relative to the pH, with a low TA/pH ratio generating a homogeneous coating microstructure with improved corrosion performance.

Chromate conversion coatings (CCCs) have been among the most successful surface treatments for light alloys, most particularly for aluminium alloys. [8,9] However their industrial application is now severely restricted as Cr(VI) is highly toxic, and classified as CMR (carcinogenic, mutagenic and reprotoxic) [10]. Trivalent chromium conversion (TCC) coatings with low toxicity and allowable environmental limits are regarded as promising alternative to CCCs [11]. TCC coatings are formed by a simple, brief dipping process, hence requiring no electrical facilities as are necessary for other common conversion treatments of magnesium alloys, such as anodizing or plasma electrolytic oxidation [12–14].

According to our knowledge one of the first studies on application of TCC coatings (SurTec 650) on AZ31B and ZE10A magnesium alloys was demonstrated by Brady et al. [15]. The coating composed of an inner Mg-F-O and an outer Zr-Cr-O layer showed the improved corrosion resistance. Potentiodynamic polarization of the alloy in saturated $Mg(OH)_2$ solution containing 1 wt.% NaCl indicated minor, if any,

* Corresponding authors.
E-mail addresses: jiantao.qi@upc.edu.cn (J. Qi), jolanta.swiatowska@chimieparistech.psl.eu (J. Światowska), peter.skeldon@manchester.ac.uk (P. Skeldon).

Table 1
Composition of AZ91D alloy by ICP-OES (wt%).

Element	Al	Cu	Fe	Mn	Ni	Si	Zn
	9.12	＜0.01	<0.004	0.18	<0.001	0.01	0.68

le

protection of the alloys.

The present work examines TCC coating formation (using a SurTec 650 bath) on AZ91D magnesium alloy. Attention is given to the role of the alloy microstructure in the development of the coating, which was

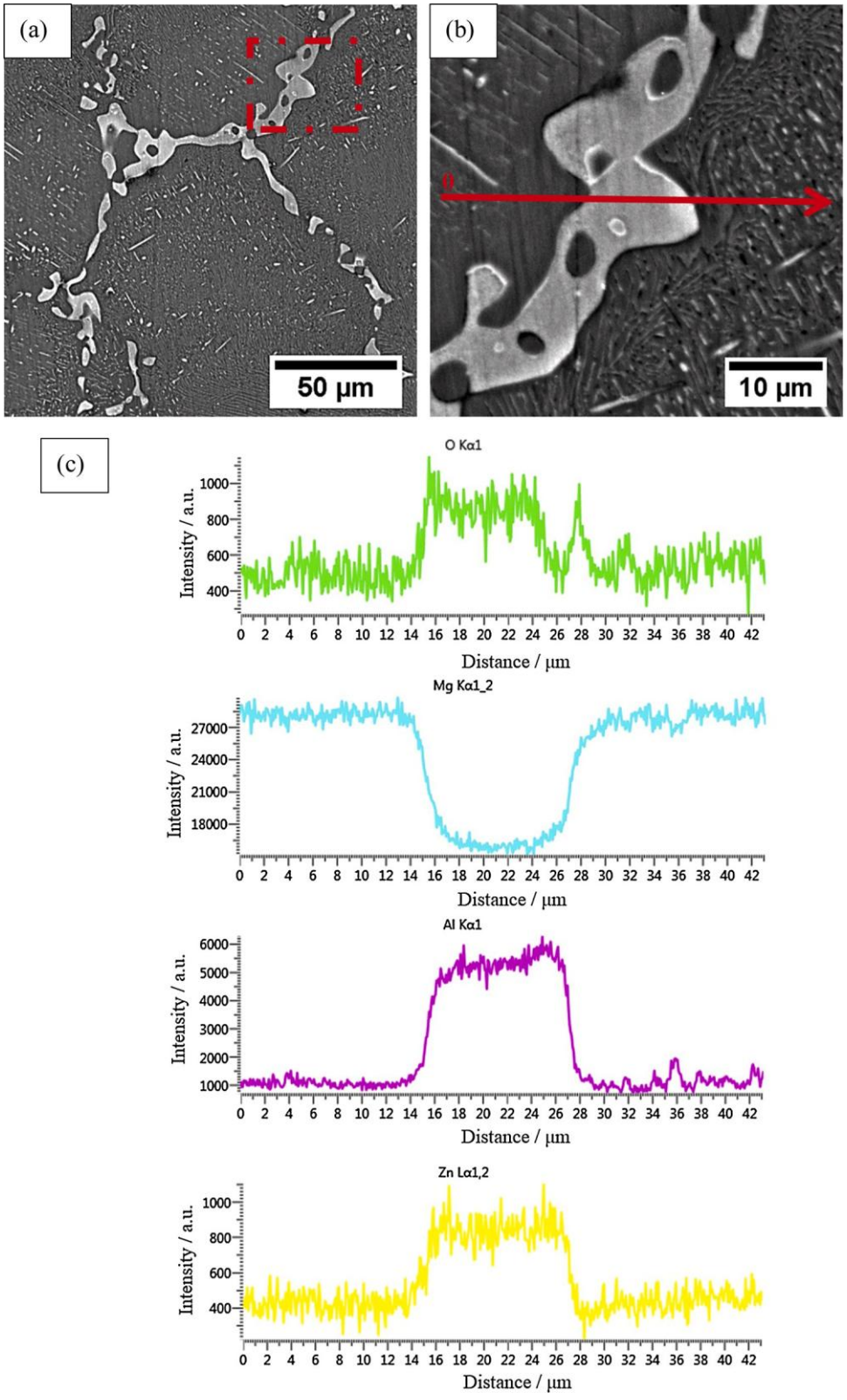

Fig. 1. (a, b) Scanning electron micrographs and (c) EDS line profiles analysis for O, Al, Mg and Zn in the pretreated bare AZ91D alloy.

not considered in the earlier investigation. The study identifies the role of the cathodic β phase ($Mg_{17}Al_{12}$) and show preferential sites for the coating deposition. The coating morphology, chemical composition and corrosion protection performance were investigated by scanning electron microscopy, X-ray photoelectron spectroscopy, Raman spectroscopy and electrochemical measurements, respectively.

2. Materials and methods

2.1. Specimen preparation

Cast AZ91D alloy (Dongguan Magnesium Alloy Material Ltd, China) was cut to provide specimens of dimensions of 15× 15×5 mm. Table 1 displays the chemical analysis of the alloy performed by ICP-OES (Optima 4300DV). The main alloying elements of the alloy are Al and Zn with 9.12 and 0.68 wt.%, respectively.

The specimens were ground to a 2000 grit SiC finish, then polished with 1.0 μm diamond paste, etched in 10 g/L NaOH + 5 g/L Na_2CO_3 at 60 °C for 10 min, deoxidized in 12.5 g/L NH_4HF_2 + 3.5 g/L glycolic acid ($C_2H_2O_3H_2O$) at 25 °C for 10 s and activated in 20 % NaOH at 25 °C for 30 min. All chemicals used for the pre-treatment were of analytical grade. Selected specimens were then TCC-coated using SurTec 650 (SurTec International Gmbh, Bensheim, Germany) solution as a bath for 10 min at 40 °C. The main constituents of SurTec 650 are chromium (III) and fluoro-zirconate salts. A previous ICP-OES of the solution by some of the present authors indicated a Zr/Cr atomic ratio of≈0.7. [16]

All specimens were finally rinsed with deionized water and dried in a cool N_2 stream. The coated specimens were stored for 15 h in laboratory air before examination. At least three specimens for each condition were prepared to ensure reproducibility. The deionized water used for solution preparation and rinsing was of resistivity < 18 Ω cm.

2.2. Electrochemical analysis

A three-electrode cell, containing a AZ91 D working electrode (area 1 cm^2), a platinum wire counter electrode (>99.99 %) and a saturated Ag/AgCl reference electrode (0.222 V *vs* SHE), with an electrochemical workstation (CS310 (Wuhan, China)), was used for electrochemical measurements. Potentiodynamic polarization scans and electrochemical impedance spectroscopy (EIS) measurements were started after 30 min immersion at the open circuit potential (OCP) in 0.05 M Na_2SO_4 solution at room temperature. EIS measurements were made from 10^5 to 10^{-2} Hz using a sinusoidal waveform of amplitude 10 mV. Anodic and cathodic polarization curves were recorded individually, starting from the OCP, at a scan rate of 1 mV/s. Electrochemical measurements were repeated at least three times to check the reproducibility.

2.3. Morphological and surface characterization

Surface morphologies and compositions before and after coating deposition were investigated by scanning electron microscopy (SEM, JSM-7200 F and Helios 5 UX) and X-ray energy dispersive spectrometry (EDS) at an accelerating voltage of 15 kV. For measurement of the coating thickness, two specimens TCC-coated for 10 min and then spray coated with carbon were glued together and mechanically polished to a 1 μm diamond finish in absolute alcohol solution. SEM/EDS was carried at 15 kV using a JSM-7200 F instrument. X-ray photoelectron spectroscopy (XPS) was performed using a Thermo ESCALAB 250XI spectrometer, with monochromatic Al Kα radiation (hυ =1486.6 eV), operated at a base pressure of≈ 10^{-10} mbar and with energy step size of 0.05 eV. Survey spectra and high-resolution spectra (C 1s, O 1s, Mg 1s, Al 2p, Cr 2p, Zr 3d, F s1 and S 2p) were recorded with a pass energy of 100 eV and 20 eV, respectively. Analyses were performed over a surface area of size 100×100 μm, with a take-off angle of 90°. Charge correction was performed with reference to the hydrocarbon peak at 285.0 eV. All data processing was carried out with the AvantageTM software (Thermo Electron Corp.) using a Shirley type background and a 70 % Gaussian 30 % Lorentzian line shape. In addition, Raman spectroscopy (Horiba LabRAM HR Evolution) was used to investigate the coating components using a 532 nm laser source, 10 % power, 100x objective lens, exposure time of 10 s and no accumulation.

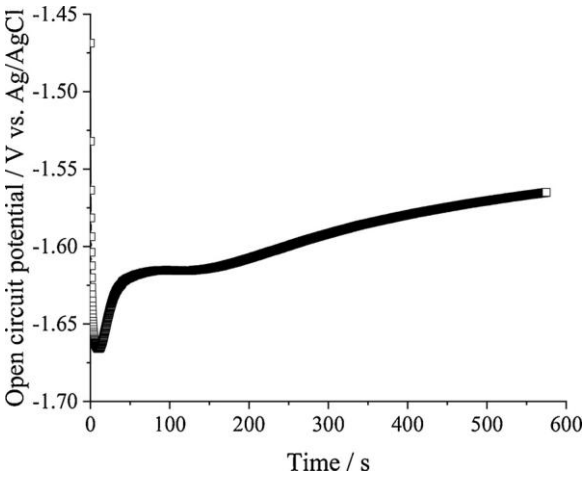

Fig. 2. Open-circuit potential-time curve for the AZ91D alloy immersed for 575 s in SurTec 650 solution at 40 °C.

3. Results and discussion

3.1. Alloy microstructure

Fig. 1 (a) displays a low magnification scanning electron micrograph of the as-pre-treated surface revealing a grain boundary phase and plate-like precipitates within the matrix. EDS analyses for Al and Mg in the boxed region of Fig. 1 (a), (shown enlarged in Fig. 1 (b)), revealed enrichment of aluminium in the grain boundary phase relative to the matrix (Fig. 1 (c)). The microstructure is consistent with grain boundary β phase ($Mg_{17}Al_{12}$) and plate-like β precipitates in the matrix similarly to previous work [1]. This β phase can be an effective cathode during corrosion of AZ91 alloy like demonstrated by Song et al. [16]. The EDS also shows the zinc enrichment at the grain boundaries β phase, and oxygen originating from the surface oxide/hydroxide layer (Fig. 1 (c)).

3.2. Coating formation and morphologies

Fig. 2 shows the OCP-time curve for the AZ91D alloy during TCC coating formation in SurTec solution at 40 °C for 575 s. Starting from an initial value of ≈1.50 V, the potential decrease by≈150 mV in the first 10 s then gradual increase to≈1.62 V by about 50 s can be observed. Thereafter, the increase is much slower, with a final potential of ≈ -1.57 V. Oxidation of magnesium and hydrogen evolution are the main electrochemical reactions. The initial variations in potential such as decrease and increase are probably due to the oxidation of the alloy (principally the attack and dissolution of the surface oxide/hydroxide layer) and the coating formation, respectively. The coating formation is promoted at cathodic β phase (shown later) and its consequential influence on the anodic and cathodic processes. The OCP evolution during TCC coating formation on magnesium alloys was similar to with that reported for aluminium and aluminium alloy. [17–19] TCC coating formation is a pH-driven process where the pH is locally increased by the cathodic reactions leading to enhanced deposition of hydroxides of chromium and zirconium. [20]

Fig. 3 (a) displays a scanning electron micrograph of a TCC-coated specimen at low magnification. The alloy surface has been covered by the TCC coating. The coating above the grain boundary β phase exhibits a network of wide cracks, which are not present in the coating above the α matrix. A region of grain boundary β phase is shown at higher

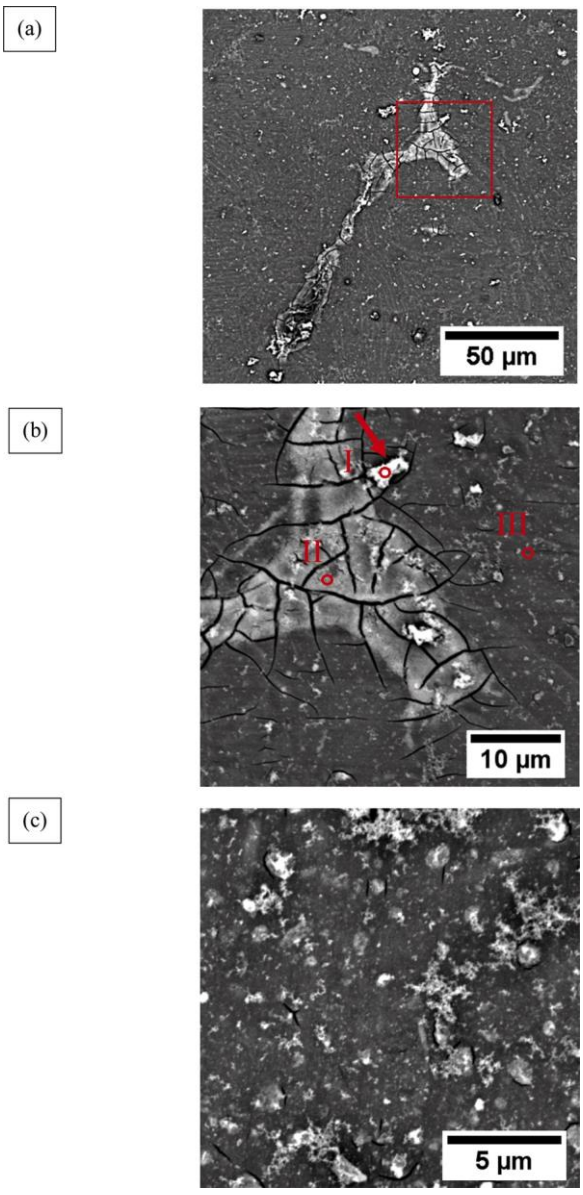

Fig. 3. Scanning electron micrographs of TCC-coated AZ91D alloy at (a) low and (b) high magnification and (c) TCC-coated α matrix.

magnification in Fig. 3 (b), and reveals the cracks propagation into the adjacent α matrix. Both the matrix and grain boundary β phase are decorated by irregularly-shaped particles, of light appearance in the micrographs (see arrows), at both the α matrix and grain boundary β phase (Fig. 3 (a, b)), with sizes from lower than 1 μm to around 10 μm.

Fig. 3 (c) shows details of the coating surface at the α matrix. The coating is decorated by fine irregular in shaper particles (as already mentioned above) and reveals short length (a few microns) fine cracks, which contrast with the continuous network of coarse cracks in the coating above the grain boundary β phase. The cracking may be due to the stress generated by shrinkage of the coating during drying in either the laboratory air or in the electron microscope.

To have a better insight into the differences in the coating composition over an irregular-shaped deposit (spot I), the grain boundary β phase (spot II) and the α matrix (spot III), the EDS analyses were performed as shown in Fig. 3 (b). The Cr/Zr atomic ratios at the respective areas were ~ 0.68, 0.52 and 0.52. The Cr/Zr ratios for the coating at the matrix and β phase grain boundary are similar to those found in TCC coatings formed on aluminium and AA 2024 alloy in a similar bath [19,

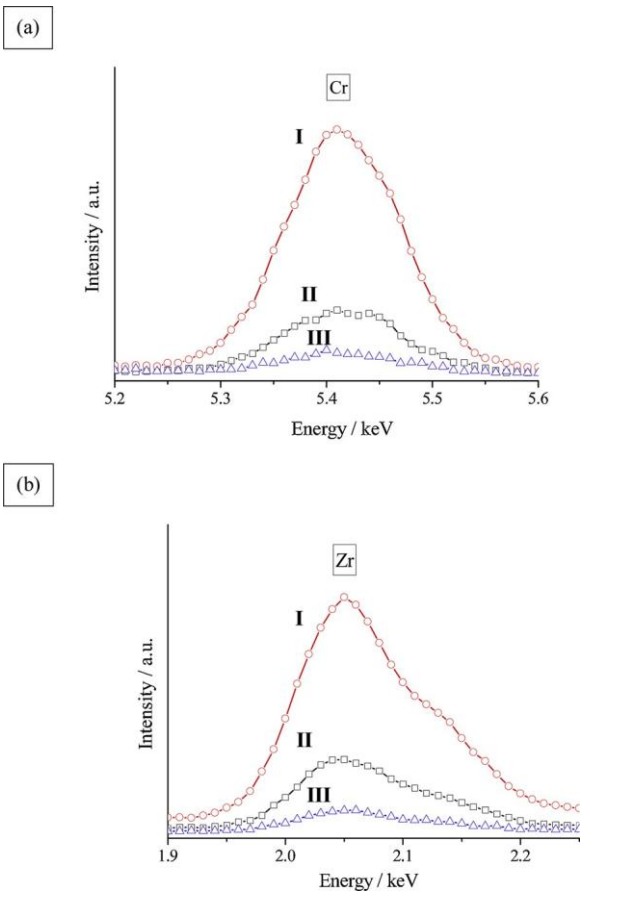

Fig. 4. EDS peaks for zirconium and chromium at spots I, II and III corresponding to over an irregular-shaped deposit, the grain boundary β phase and the α matrix, respectively, shown in Fig. 3b.

21]. Fig. 4 (a, b) shows the intensities of the chromium and zirconium peaks at these different areas I, II and III. The intensities of both peaks decreased in order I > II > III. The highest signals at region I are due to the large size and thickness of the irregularly-shaped particle relative to the comparatively thin TCC coating layers on the grain boundary β phase than at the α matrix. The chromium and zirconium peaks are about 3 times higher at the β phase site compared with the α matrix region, which is consistent with a greater coating thickness at the former region.

The coating was examined in cross-section using backscattered electrons (Fig. 5). The coating above the alloy matrix (Fig. 5 (a)) revealed an outer layer of light appearance, with a thickness of 50 nm, and an inner, darker layer of thickness ≈ 40 nm. The thickness of the inner layer in particular was locally variable by up to a factor of 2. The pore like-features of the inner layer are possibly the result of irradiation damage or dehydration by the electron beam. The outer layer contained chromium and zirconium, giving rise to enhance electron scattering compared with the inner, magnesium-rich layer. The coating above a region of β phase was similarly two-layered (Fig. 5 (b)), with a thicker outer layer than above the matrix, ≈ 75 nm. The thickness of the inner layer above the β phase was similar to that above the matrix. The difference between the coating thickness on the α matrix and β phase in the cross-sections is less significant than was deduced from the EDS analysis,

which may be related to a variable thicknesses over different β phase regions. The higher thickness of the coating over the grain boundary β phase may be explained by the cathodic activity (oxygen reduction and hydrogen evolution) and large area of the β phase. The cathodic reactions result in a pH increase in the solution adjacent to the specimen surface. The interfacial pH can also be increased due to the solubility of $Mg(OH)_2$ formed by the oxidation of the alloy. The principle

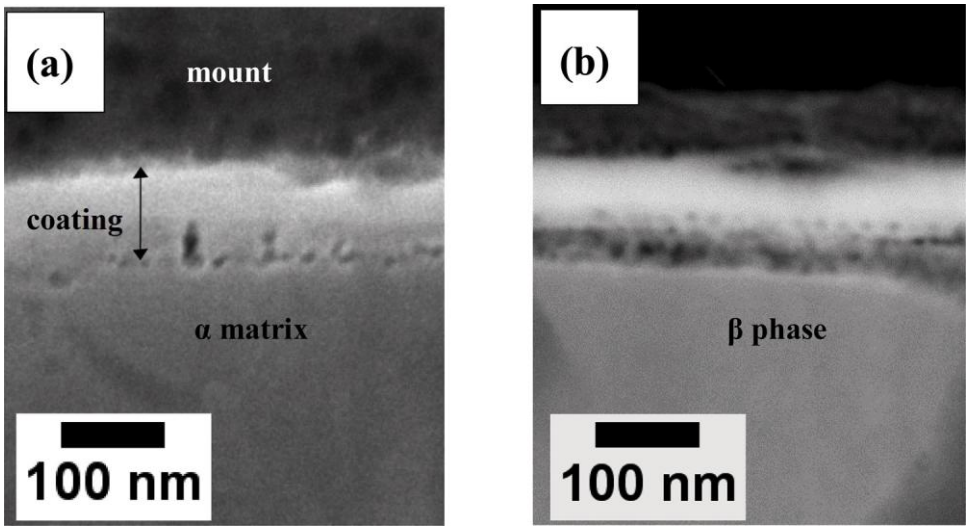

Fig. 5. Backscattered electron scanning electron micrographs of a cross-section of the TCC-coated AZ91D alloy. (a) α matrix and (b) β phase.

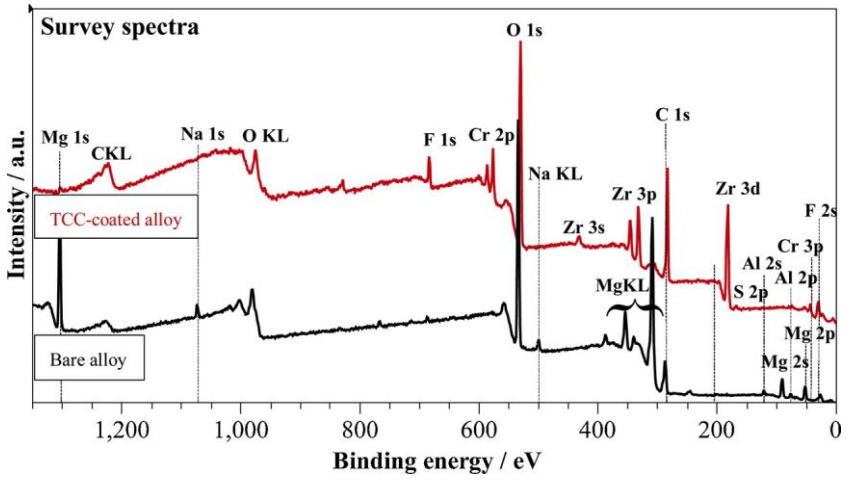

Fig. 6. XPS survey spectra for pretreated (bare) and TCC-coated AZ91D alloy.

components of the deposited coating material (shown later by XPS) consist of ZrO_2 and hydrated Cr(III) species ($Cr(OH)_3$/CrOOH) species, which are formed by the reactions:

$$ZrF_6^{2-} + 4OH^- \rightarrow ZrO_2 + 6F^- + 2H_2O \quad (1)$$

$$Cr^{3+} + 3OH^- \rightarrow Cr(OH)_3 \quad (2)$$

The greater in crease in pH at the grain boundary β phase may be explained by the increased deposition of coating components relative to that at the α matrix. Beneath the deposited layer a thinner Mg-F-O layer can be formed due to the anodic oxidation of magnesium as shown by Brady et al. [12].

3.3. *Chemical characterization by XPS and raman spectroscopy*

Chemical surface characterization of specimens with and without TCC coating was performed by XPS (Fig. 6). Owing to the size of the analyzed area of the specimen surfaces (500 μm^2), the XPS analyses provide compositions averaged over regions of both α and β phases to a depth of ≈5–10 nm. Fig. 6 compares the survey spectra of the two specimens pretreated (bare) and TCC-coated AZ91D alloy. Carbon, which was detected on both the bare and coated alloy, could originate from chemicals used in the pre-treatment and coating processes and from adsorption of organic species in the laboratory atmosphere. A detailed decomposition of the C 1s core level region for both specimens is presented in Fig. 7a and d. As shown in Fig. 7a, four peaks were distinguished: C-C at 285.0 eV (FWHM =2.0 eV), C-O at 286.6 (FWHM =1.9 eV), O-C = O at 288.6 eV (FWHM =1.9 eV) and —CO_3 at 290.8 eV (FWHM =1.9 eV). After TCC treatment (Fig. 7d), the carbon peak showed only three contributions: C-C, C-O and O-C = O. and the carbonate species (–CO_3) were not observed.

The alloy substrate before TCC treatment (bare alloy in Fig. 6) showed principally the presence of aluminium and magnesium oxy-hydroxides due to the surface pre-treatment. The presence of aluminium and magnesium oxides and/or hydroxides was confirmed by the in-depth characterization of the high resolution Al 2p and Mg 1 s spectra, respectively (present in Fig. 7b and c). The Al 2p core level region shows one peak at 75.6 eV (FWHM=2.8 eV) corresponding to aluminium oxide or hydroxide (Al^{3+}) [18,22,23] and the Mg 1 s a peak at 1304.3 eV (FWHM=3.5 eV), which can be attributed to magnesium oxide/hydroxide (Mg^{2+}) [24,25]. The large quantity of $MgO/Mg(OH)_2$ species can be revealed by the high intensity of the Mg 1 s peak, the other core levels peaks such as Mg 2p (at around 49 eV) and Mg 2 s (at around 86 eV) as well as series of Mg Auger peaks between 300–390 eV. After the formation of the TCC conversion layer (Fig. 6), the Al 2p and Mg 1 s peaks are significantly attenuated (as also showed by the surface composition presented in Table 2) indicating the formation of the

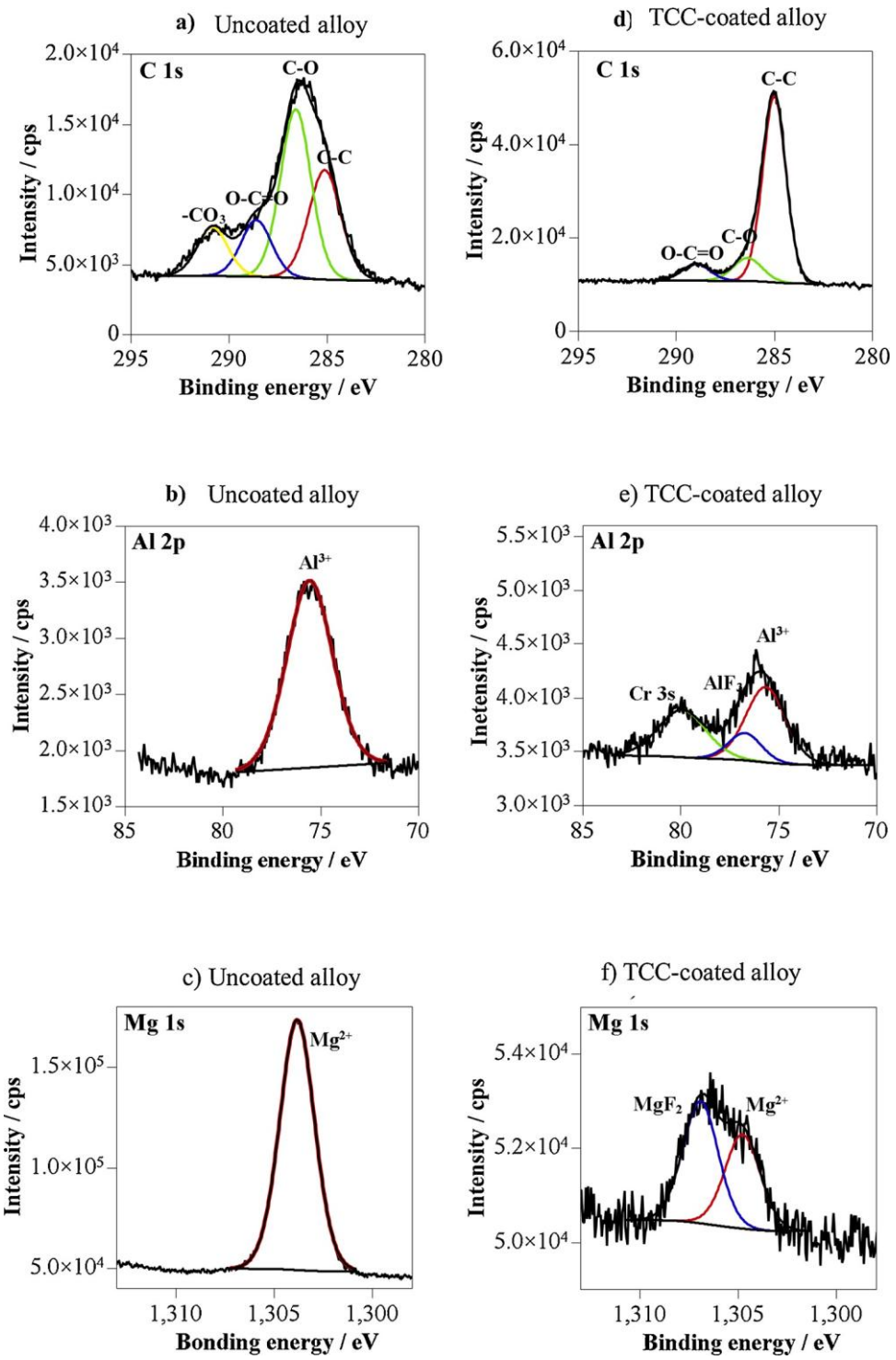

Fig. 7. High resolution XPS C 1s, Al 2p and Mg 1s core level spectra (a, b, c) for pretreated bare AZ91D alloy; (d, e, f) for pretreated and TCC-coated AZ91D alloy.

Table 2
Elemental concentrations (at.%) for pretreated bare and TCC-coated AZ91D alloy from XPS. The coating was formed in SurTec 650 solution at 40 °C for 600 s.

Element	Al	S	Zr	O	Cr	F	Mg
Bare alloy	5.0	/	/	70.2	/	/	24.8
TCC-coated alloy	4.2	1.2	12.7	67.1	6.3	7.0	2.6

conversion layer.

The high resolution Al 2p and Mg 1 s spectra for the TCC converted sample are presented in Fig. 7e and f, respectively. The lowest binding energy peaks corresponding to aluminium (Al^{3+}) and magnesium (Mg^{2+}) oxy-hydroxides are still present but they show much lower intensities than on the bare alloy (Fig. 6b and c). New components appeared in the Al 2p peak at 76.7 eV (FWHM =2.1 eV) and 80.0 eV (FWHM =2.9 eV) corresponding to AlF_3 [18,26] and Cr 3 s, respectively. Formation of AlF_3 can originate from the surface pretreatment or the conversion treatment bath. Low amounts of fluorine, and also sodium,

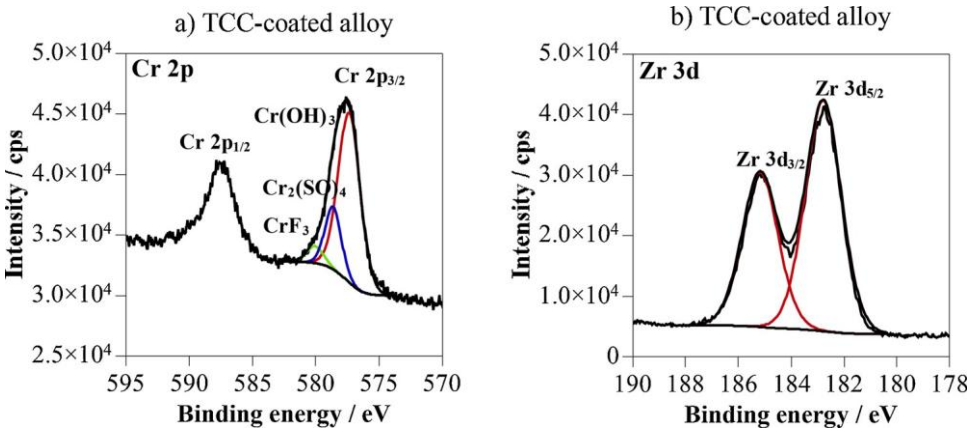

Fig. 8. High resolution XPS Cr 2p and Zr 3d core level spectra for TCC-coated AZ91D alloy.

Table 3
Components (%) of TCC coating formed on AZ91D alloy in SurTec 650 solution at 40 °C for 600 s, from XPS (using Cr/Zr at. ratio in Table 2).

Compound	$Cr(OH)_3$	$Cr_2(SO_4)_3$	CrF_3	ZrO_2
	24	2	6	68

were observed on the uncoated alloy (Fig. 6). The presence of AlF_3 has been observed on TCC-coated AA2024 alloy [18]. The appearance of Cr 3 s in the region of Al 2p core level peak corroborates with the presence of a coating containing Cr and Zr species, as discussed below.

A major difference observed in the survey spectra for the TCC treated specimen with reference to the non-converted is the appearance of peaks corresponding to zirconium (Zr 3d and other core level peaks Zr 3p and Zr 3 s) and chromium (Cr 2p, and also Cr 3p) (Fig. 6). The Cr/Zr atomic ratio is ~0.49 (Table 2). A decomposition of two principal Cr (Cr 2p) and Zr (Zr 3d) peaks is presented in Fig. 8. Other coating components are fluoride and sulfur, as evidenced by presence of F 1 s and S 2p peaks, respectively. The surface elemental compositions for both samples are present in Table 3. The high at% of O 1s (Table 2) can be related not only to the presence of Cr and Zr oxides and hydroxides but also to the presence of oxygenated carbon-like contamination detected on both specimens as explained in the decomposition of the C1 s peak. The quantitative analysis of the surface composition was performed based on the high resolution spectra assuming a uniform and homogeneous surface layer for both the as-pretreated alloy and for the alloy after formation of the TCC conversion layer. The carbon-containing contamination was not taken into account for this analysis. The small amount of sodium and fluoride contamination on the surface of bare alloy was also neglected in the quantitative analysis of the surface composition.

Fig. 8 presents high resolution Cr 2p (a) and Zr 3d (b) spectra obtained for the TCC converted sample. The Cr 2 p spectrum shows a spin orbit doublet with two well-separated peaks, Cr $2p_{3/2}$ and Cr $2p_{1/2}$ (with Δ BE 9.8 eV). As reported previously [27], a decomposition and interpretation of Cr 2p core level spectra in the case of chromium (III) oxides is quite difficult due to presence of a multiplet splitting in the 2p state of Cr(III) oxides [28,29]. The chromium (III) hydroxides, showed only one but broad peak as reported by Biesinger et al. [30]. The interpretation of Cr valence states is also hindered by the similar binding energies of Cr(III) components corresponding to hydroxides and fluorides and Cr(VI) components corresponding to oxides [21,31].

Due to the clear separation of Cr $2p_{3/2}$ and Cr $2p_{1/2}$ peaks, only a principal Cr $2p_{3/2}$ peak was decomposed here, as presented in Fig. 8a. Three components can be distinguished: a principal symmetric peak at 577.4 eV (FWHM=2.1 eV), which is assigned to $Cr(OH)_3$ and/or CrOOH [32,33], and two lower intensity peaks at higher binding energies at

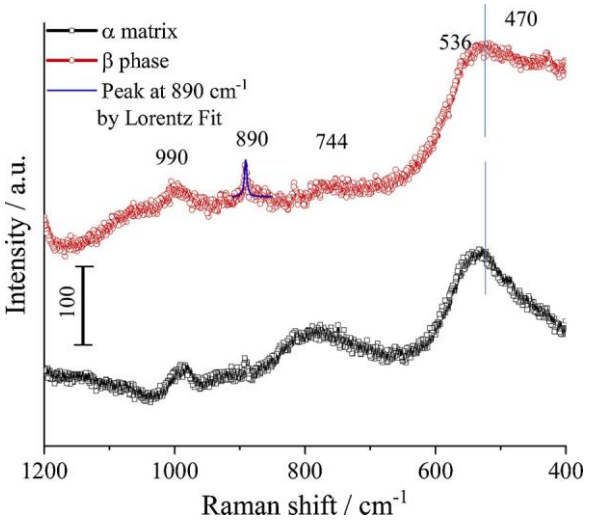

Fig. 9. Raman spectra of TCC-coated α matrix and β phase in AZ91D alloy.

578.6 eV (FWHM =1.6 eV) and at 580.1 eV (FWHM =2.1 eV) attributed to $Cr_2(SO_4)_3$ and CrF_3, respectively. The binding energy of the principal peak is in good agreement with XPS data for $Cr(OH)_3$ and CrOOH in the literature [28,29,34–36]. The chromium fluoride at a similar binding energy was also previously observed on converted AA2024 [18,21,37]. Similarly, to CrF_3, the presence of $Cr_2(SO_4)_3$ was also detected on the conversion coating deposited on aluminium alloy [38]. The formation of a small quantity of Cr(VI) species cannot be completely ruled out, due to possible overlapping with a peak corresponding to CrF_3. Depending on the reference, the binding energy of Cr(VI) species has been reported to be between 579.5 and 580.2 eV and Cr(III) attributed to CrF_3 between 579.3 and 580.8 eV [32]. The presence of fluorides and sulphates can be confirmed by F 1 s (with a peak at around 685.9 eV) and S 2p (at around 168.8 eV) peaks, not shown here as high resolution spectra. A high intensity F 1 s peak clearly observed on a survey spectrum (Fig. 5), cannot be explained only by the presence of a small quantity of CrF_3. As already discussed above, low intensity peaks attributed to AlF_3 and MgF_2 were also detected. However, it can be inferred from the intensity of the F 1s peak that the highest binding energy Cr 2p peak at 580.1 eV mostly originates from Cr(III) associated with F than Cr(VI) with O. As explained above, the stoichiometric analysis of Cr(VI)-O using O 1s core level peak can be difficult due to overlapping of Cr(VI)-O species and C-O- or Zr-O related species.

The Zr 3d spectrum (Fig. 8) shows a Zr $3d_{5/2}$ and Zr $3d_{3/2}$ spin-orbit doublet at binding energies of 182.8 and 185.2 eV (with FWHM =1.7 eV

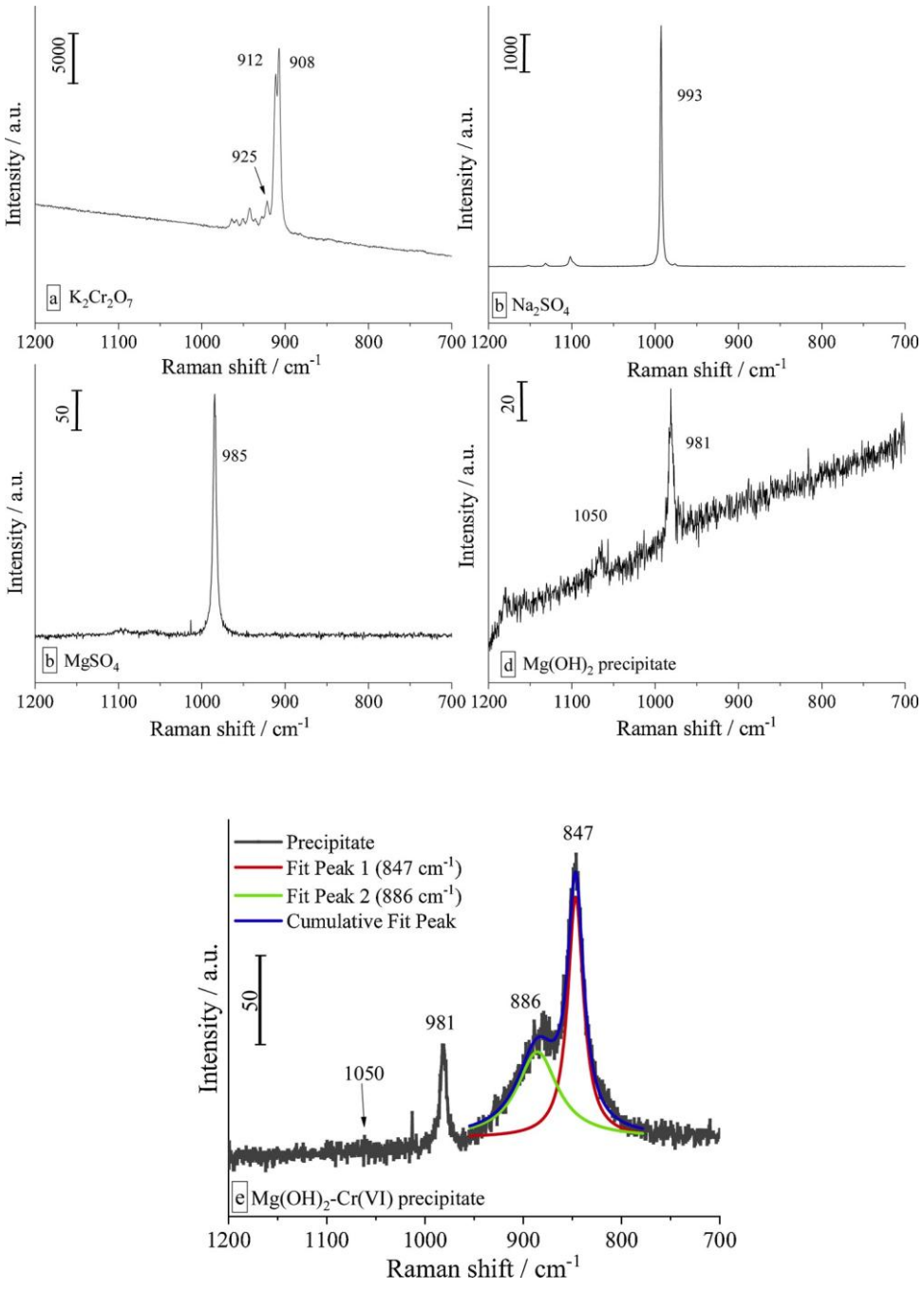

Fig. 10. Raman spectra for (a) $K_2Cr_2O_7$, (b) Na_2SO_4, (c) $MgSO_4$, (d) $Mg(OH)_2$ and (e) $Mg(OH)_2$-Cr(VI) precipitates.

for both peaks). The fitting of the $Zr_{5/2}$ peak indicated the presence of ZrO_2 at a binding energy in agreement with previous results [18,39]. No ZrF_4 species were detected by XPS in the conversion coating. Table 3 reports the atomic percentages of chromium and zirconium ions (i.e. Cr/(Cr + Zr)% and Zr/(Cr + Zr)%) associated with $Cr(OH)_3$/CrOOH), $Cr_2(SO_4)_3$, CrF_6 and ZrO_2. The coating also contains lower amounts of other constituents, such as aluminium and magnesium species in the form of oxide, hydroxide or fluoride.

To further investigate the chemical composition of the TCC-coating on the AZ91D alloy Raman spectroscopy was employed. The spectrum (Fig. 9) show fingerprints of ZrO_2, MgF_2 and SO_4^{2-} ions at Raman shifts of 470, 744 and 990 cm^{-1}, respectively [19,40]. A broad peak at ≈ 530 cm^{-1} is attributed to $Cr(OH)_3$ and/or Cr_2O_3, which have Raman shifts at 526 and 536 cm^{-1}, respectively [41]. Although Cr_2O_3 was not identified by XPS, it might exist at depths greater than the escape depth of the photoelectrons, or have been produced by dehydration of hydrated Cr (III) species under the laser irradiation.

A further peak at 890 $cm^{-1}$is assigned to Cr(VI) species. The peak was of higher intensity at the β phase than the α matrix. In support of the assignment, Raman spectra were acquired for (i) $K_2Cr_2O_7$ (Fig. 10(a)), (ii) Na_2SO_4 (Fig. 10 (b)), $MgSO_4$ (Fig. 10 (c)), (iii) $Mg(OH)_2$ precipitate formed in 0.25 M $MgSO_4$, with the pH adjusted to 10 by droplets of NaOH solution (Fig. 10 (d)) and $Mg(OH)_2$-Cr(VI) precipitate formed in 0.25 M $K_2Cr_2O_7$/0.5 M $MgSO_4$ solution after adjustment to pH 10 by droplets of NaOH solution. (Fig. 10 (e)). The precipitates in Figs. 10 (d, e) were filtered, rinsed in deionized water and dried. Peaks at 912, 908 cm^{-1} are assigned to $Cr_2O_7^{2-}$ (Fig. 10 (a)) and at 985 and 993 cm^{-1} to SO^{2-} (Fig. 10 (b, c) [41,42]. A peak due to sulphate residues is also evident for the precipitate. The O–H band was observed at 1050 cm^{-1} with sulphate residues at 981 cm^{-1} in Fig. 10d [43]. The peak at 847

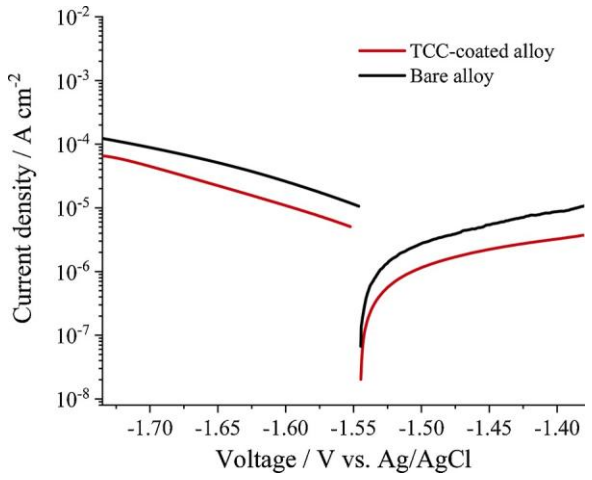

Fig. 11. Anodic and cathodic potentiodynamic polarization curves for the pre-treated (bare) and TCC-coated AZ91D alloy specimens in 0.05 M Na_2SO_4 solution.

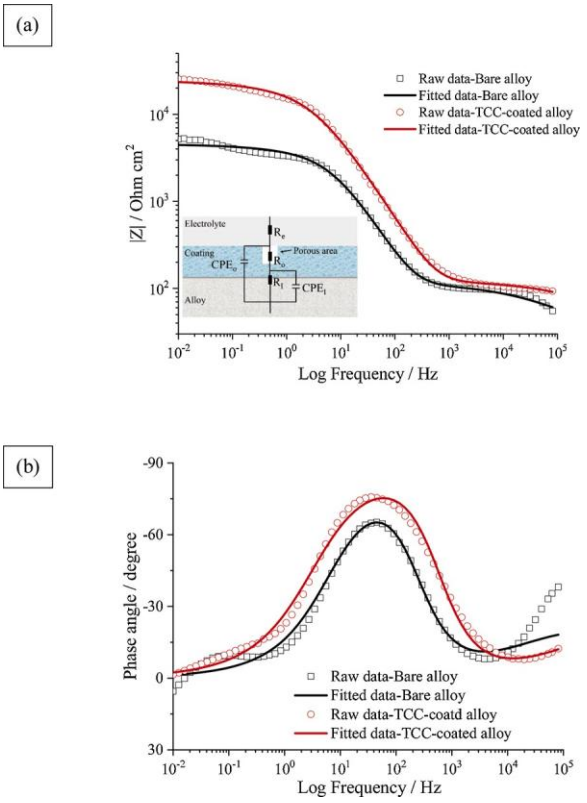

Fig. 12. EIS for pretreated bare AZ91D alloy (□) and TCC-coated AZ91D alloy (○) specimens in 0.05 M Na_2SO_4 solution: (a) |Z|-frequency and (b) phase angle-frequency.

cm^{-1} for $Mg(OH)_2$-Cr(VI) is in agreement the reported value for CrO_4^{2-} species [40]. The peak at 886 cm^{-1} peak is assigned to $Cr_2O_7^{2-}$ and/or $HCrO_4$- species, with the shift influenced by the presence of Mg(II) and possibly Na(I) species. $HCrO_4$- have been previously assigned a Raman shift of 899 cm^{-1} [44]. Using mixed oxides containing Cr (VI) and Cr(III) or Al(III), others have shown that the Raman shift depends on the Cr(VI) environment [41,45].

Table 4
Fitted electrochemical impedance spectroscopy parameters obtained for pre-treated bare and TCC-coated AZ91D alloy.

	Bare alloy	TCC-coated alloy
R_e (Ω cm^2)	18 ± 2	18 ± 1
CPE_O ($\mu S s^{-2} cm^{-2}$)	27 ± 5.3	4.3 ± 1.8
R_O (Ω cm^2)	100 ± 11	106 ± 12
CPE_I ($\mu S s^{-2} cm^{-2}$)	5.7 ± 1.3	2.2 ± 0.9
R_I (Ω cm^2)	4436 ± 121	24,359 ± 150

3.4. Electrochemical characterization

In order to demonstrate the barrier properties of the TCC coating deposited on the pre-treated AZ91D alloy, potentiodynamic polarization and electrochemical impedance spectroscopy were performed in 0.05 M Na_2SO_4 solution. Cathodic and anodic polarization curves (Fig. 11) reveal the reduced current density by a factor of 2 relative to that of the uncoated specimen. The curves showed no well-defined Tafel regions to determine the corrosion current density at the corrosion potential.

Fig. 12 (a, b) displays typical examples of Bode plots of EIS data for uncoated and TCC-coated specimens. The data were fitted with an equivalent circuit (inset in Fig. 12) that represents a barrier coating comprising an outer ZrO_2/$Cr(OH)_3$/CrOOH layer and an inner Mg-F-O layer, the latter reported by Brady et al. [15]. The components of the equivalent circuit are R_e the electrolyte resistance, R_O and R_I – the resistances of the outer and inner layers, and CPE_O and CPE_I are constant phase elements for the respective layers. Since a film consisting of an outer hydroxide layer and inner oxide layer has been reported to form in Na_2SO_4 solution [46], a similar equivalent circuit was employed to the pretreated specimens. CPEs replaced capacitances due to the non-ideal behavior of the layers on both uncoated and coated specimens. The average and standard deviations of each circuit element derived from fitting of the data in triplicated tests are listed in Table 4.

The outer layers of the pre-treated and TCC-coated AZ91D alloy specimens show similar resistances of ≈ 100 Ω cm^2. In contrast, the resistances of the inner layers of the respective specimens were significantly higher, namely 4.4 10^3 Ω and 2.4 10^4 Ω cm^2. Thus, the inner Mg-F-O layer of the TCC coat provided the main protection, with a resistance about 5 times that of the uncoated specimen. The higher CPEs of the inner and outer layers of the TCC-coated specimen suggest greater layer thicknesses compared with those of the uncoated alloy. The low resistance of the outer layer may be caused by defects in the coating, such as cracks or cavities, or easy transport of species through the coating, for instance due to a gel-like structure. In practice, it is expected that the TCC coating would be applied beneath an organic coating in part of a protection scheme that would provide corrosion resistance in more aggressive environments, for instance when chloride ions are present.

4. Conclusions

TCC coating of AZ91B alloy results in deposition of coating material above both the α matrix and the β phase. A thicker layer is produced at the cathodic grain boundary β phase compared with the α matrix owing to a greater pH rise at the former location that results from reduction of oxygen and H^+ ions.

The atomic ratio of chromium to zirconium in the coating was approximately 0.5. $Cr(OH)_3$/CrOOH, $Cr_2(SO_4)_3$, CrF_3 and ZrO_2 species were main components of the deposited coating material. Cr(VI) was also present, particularly in the coating above cathodic β phase. The Cr(VI) was generated by oxidation of Cr(III) by H_2O_2 produced by reduction of oxygen

Electrochemical impedance spectroscopy and potentiodynamic polarization revealed that the TCC coating provided a barrier to corrosion of the alloy. The protection was mainly due to an inner Mg-rich layer

layer of the coating located beneath the less protective deposited layer.

Author statement

Jiantao Qi carried out the data curation and writing-Original draft preparation;

Zonghao Ye carried out the sample preparation and microstructure investigation;

Ning Gong carried out the Raman sample preparation and investigation;

Xuelian Qu carried out the electrochemical measurement;

Dimitri Mercierc provided the electrochemical methodology and validation;

Jolanta Świątowskac carried out the XPS data analyses and paper reviewing and editing;

Peter Skeldond carried out the paper writing-reviewing and editing;

Philippe Marcusc provided the paper writing-reviewing and editing;

Declaration of Competing Interest

The authors declare that they have no known competing financial interests or personal relationships that could have appeared to influence the work reported in this paper.

Acknowledgements

The following are acknowledged for support: National Natural Science Foundation of China (51701239), Fundamental Research Funds for the Central Universities (18CX02128A) and Graduate Innovation Project from China University of Petroleum (East China) (YCX2020093). The authors also wish to thank Dr. Changrun Cai, of Nanoport, Thermo Fisher Scientific (Shanghai, China) for assistance with SEM.

References

[1] A. Kiełbus, R. Jarosz, A. Gryc, Effect of modification on microstructure and properties of AZ91 magnesium alloy, Crystals 10 (2020) 536.

[2] A. Zarebidaki, H. Mahmoudikohani, M.-R. Aboutalebi, Microstructure and corrosion behavior of electrodeposited nano-crystalline nickel coating on AZ91 Mg alloy, J. Alloys. Compd. 615 (2014) 825–830.

[3] L. Yang, X. Zhou, M. Curioni, S. Pawar, H. Liu, Z. Fan, G. Scamans, G. Thompson, Corrosion behavior of pure magnesium with low iron content in 3.5 wt% NaCl solution, J. Electrochem. Soc. 162 (2015) C362–C368.

[4] H. Huo, Y. Li, F. Wang, Corrosion of AZ91D magnesium alloy with a chemical conversion coating and electroless nickel layer, Corros. Sci. 46 (2004) 1467–1477.

[5] G. Duan, L. Yang, S. Liao, C. Zhang, X. Lu, Y. Yang, B. Zhang, Y. Wei, T. Zhang, B. Yu, X. Zhang, F. Wang, Designing for the chemical conversion coating with high corrosion resistance and low electrical contact resistance on AZ91D magnesium alloy, Corros. Sci. 135 (2018) 197–206.

[6] W. Zai, Y. Su, H.C. Man, J. Lian, G. Li, Effect of pH value and preparation temperature on the formation of magnesium phosphate conversion coatings on AZ31 magnesium alloy, Appl. Surf. Sci. 492 (2019) 314–327.

[7] Z. Chunyan, L. Shangju, Y. Baoxing, L. Xiaopeng, C. Xiao-Bo, Z. Tao, W. Fuhui, Ratio of total acidity to pH value of coating bath: a new strategy towards phosphate conversion coatings with optimized corrosion resistance for magnesium alloys, Corros. Sci. 150 (2019) 279–295.

[8] S. Gheytani, Y. Liang, Y. Jing, J.Q. Xu, Y. Yao, Chromate conversion coated aluminium as a light-weight and corrosion-resistant current collector for aqueous lithium-ion batteries, J. Mater. Chem. A Mater. Energy Sustain. 4 (2016) 395–399.

[9] Y. Liu, P. Skeldon, G.E. Thompson, H. Habazaki, K. Shimizu, Chromate conversion coatings on aluminium-copper alloys, Corros. Sci. 47 (2005) 341–354.

[10] M.W. Kendig, R.G. Buchheit, Corrosion inhibition of aluminum and aluminum alloys by soluble chromates, chromate coatings, and chromate-free coatings, Corrosion 59 (2003) 379–400.

[11] D.B. Mitton, A. Carangelo, A. Acquesta, T. Monetta, M. Curioni, F. Bellucci, Selected Cr(VI) replacement options for aluminum alloys: a literature survey, Corro. Rev. 35 (2017) 365–381.

[12] B. Mingo, Y. Guo, A. Němcová, A. Gholinia, M. Mohedano, M. Sun, A. Matthews, A. Yerokhin, Incorporation of halloysite nanotubes into forsterite surface layer during plasma electrolytic oxidation of AM50 Mg alloy, Electrochim. Acta 299 (2019) 772–788.

[13] Z. Chen, H. Ji, X. Geng, X. Chen, X. Yong, S. Zhang, 3-D distribution characteristics of the micro-defects in the PEO coating on ZM6 mg-alloy during corrosion, Corros. Sci. 174 (2020), 108821.

[14] H.-Y. Hsiao, W.-T. Tsai, Characterization of anodic films formed on AZ91D magnesium alloy, Surf. Coat. Technol. 190 (2005) 299–308.

[15] M.P. Brady, D.N. Leonard, H.M. Meyer Iii, J.K. Thomson, K.A. Unocic, H. H. Elsentriecy, G.L. Song, K. Kitchen, B. Davis, Advanced characterization study of commercial conversion and electrocoating structures on magnesium alloys AZ31B and ZE10A, Sur. Coat. Technol. 294 (2016) 164–176.

[16] G. Song, A. Atrens, X. Wu, B. Zhang, Corrosion behaviour of AZ21, AZ501 and AZ91 in sodium chloride, Corros. Sci. 40 (1998) 1769–1791.

[17] X. Verdalet-Guardiola, B. Fori, J.-P. Bonino, S. Duluard, C. Blanc, Nucleation and growth mechanisms of trivalent chromium conversion coatings on 2024-T3 aluminium alloy, Corros. Sci. 155 (2019) 109–120.

[18] R. Viroulaud, J. Świątowska, A. Seyeux, S. Zanna, J. Tardelli, P. Marcus, Influence of surface pretreatments on the quality of trivalent chromium process coatings on aluminum alloy, Appl. Surf. Sci. 423 (2017) 927–938.

[19] J.T. Qi, T. Hashimoto, J.R. Walton, X. Zhou, P. Skeldon, G.E. Thompson, Trivalent chromium conversion coating formation on aluminium, Surf. Coat. Technol. 280 (2015) 317–329.

[20] L. Li, A.L. Desouza, G.M. Swain, In situ pH measurement during the formation of conversion coatings on an aluminum alloy (AA2024), Analyst 138 (2013) 4398–4402.

[21] J. Qi, T. Hashimoto, J. Walton, X. Zhou, P. Skeldon, G.E. Thompson, Formation of a trivalent chromium conversion coating on AA2024-T351 alloy, J. Electrochem. Soc. 163 (2016) C25–C35.

[22] K. Domen, T.J. Chuang, Laser induced photodissociation and desorption. I. CH_2I_2 adsorbed on Al_2O_3, J. Chem. Phys. 90 (1989) 3318.

[23] I. Olefjord, H.J. Mathieu, P. Marcus, Intercomparison of surface analysis of thin aluminium oxide films, Surf. Interface Anal. 15 (1990) 681–692.

[24] S.C. Stuart, E. Satchet, A. Sandin, J.P. Maria, J.E. Rowe, D.B. Dougherty, M. Ulrich, Smooth MgO films grown on graphite and graphene by pulsed laser deposition, J. Vac. Sci. Technol. B 31 (2013), 051804.

[25] L. Savio, E. Celasco, L. Vattuone, M. Rocca, Enhanced reactivity at metal oxide interface: water interaction with MgO ultrathin films, J. Phys. Chem. B 108 (2004) 7771–7778.

[26] R.G. Haverkamp, J.B. Metson, M.M. Hyland, B.J. Welch, Adsorption of hydrogen fluoride on alumina, Surf. Interface Anal. 19 (1992) 139–144.

[27] M. Ely, J. Świątowska, A. Seyeux, S. Zanna, P. Marcus, Role of post-treatment in improved corrosion behavior of trivalent chromium protection (TCP) coating deposited on aluminum alloy 2024-T3, J. Electrochem. Soc. 164 (2017) C276–C284.

[28] A.R. Pratt, N.S. McIntyre, Comment on 'Curve fitting of Cr 2p photoelectron spectra of Cr_2O_3 and CrF_3', Surf. Interface Anal. 24 (1996) 529–530.

[29] M. Aronniemi, J. Sainio, J. Lahtinen, Chemical state quantification of iron and chromium oxides using XPS: the effect of the background subtraction method, Surf. Sci. 578 (2005) 108–123.

[30] M.C. Biesinger, B.P. Payne, A.P. Grosvenor, L.W.M. Lau, A.R. Gerson, R.S.C. Smart, Resolving surface chemical states in XPS analysis of first row transition metals, oxides and hydroxides: Cr, Mn, Fe, Co and Ni, Appl. Surf. Sci. 257 (2011) 2717–2730.

[31] C.D. Wagner, W.M. Riggs, L.E. Davis, J.F. Moulder, G.E. Muilenberg, Handbook of X-ray Photoelectron Spectroscopy. Perkin-elmer Corporation, Physical electronics division, USA, 1978.

[32] Q. Liu, H. Liu, H. Chen, X. Wang, D. Hu, X. Cheng, H. Xu, Thermodynamic investigation with chemical kinetic analysis on the reoxidation phenomenon of the Cr(iii) in air, RSC Adv. 10 (2020) 27775–27787.

[33] A.R. Brooks, C.R. Clayton, K. Doss, Y.C. Lu, On the role of Cr in the passivity of stainless steel, J. Electrochem. Soc. 133 (1986) 2459–2464.

[34] A.E. Hughes, R.J. Taylor, B.R.W. Hinton, Chromate conversion coatings on 2024 Al alloy, Surf. Interface Anal. 25 (1997) 223–234.

[35] B. Stypula, J. Stoch, The characterization of passive films on chromium electrodes by XPS, Corros. Sci. 36 (1994) 2159–2167.

[36] W.P. Yang, D. Costa, P. Marcus, Resistance to pitting and chemical composition of passive films of a Fe-17%Cr alloy in chloride-containing acid solution, J. Electrochem. Soc. 141 (1994) 2669.

[37] T. Gross, D. Treu, E. Ünveren, E. Kemnitz, W.E.S. Unger, Characterization of Cr(III) compounds of O, OH, F and Cl by XPS, Surf. Sci. Spectra. 15 (2008) 77–123.

[38] P. Campestrini, G. Goeminne, H. Terryn, J. Vereecken, J.H.W. de Wit, Chromate conversion coating on aluminum alloys - I. Formation mechanism, J. Electrochem. Soc. 151 (2004) B59–B70.

[39] S. Sinha, S. Badrinarayanan, A.P.B. Sinha, Interaction of oxygen with $Zr_{76}Fe_{24}$ metglass: an X-ray photoelectron spectroscopy study, J. Less-Common Met. 125 (1986) 85–95.

[40] M.L. Lesiecki, J.W. Nibler, Infrared and Raman spectra and structures of matrix isolated magnesium dihalides: MgF2, MgCl2, MgBr2, and MgI2, J. Chem. Phys. 64 (1976) 871–884.

[41] L.L. Li, D.Y. Kim, G.M. Swain, Transient formation of chromate in trivalent chromium process (TCP) coatings on AA2024 as probed by Raman spectroscopy, J. Electrochem. Soc. 159 (2012) C326–C333.

[42] J. Qi, J. Walton, G.E. Thompson, S.P. Albu, J. Carr, Spectroscopic studies of chromium VI formed in the trivalent chromium conversion coatings on aluminum, J. Electrochem. Soc. 163 (2016) C357–C363.

[43] A. Maltseva, S.V. Lamaka, K.A. Yasakau, D. Mei, D. Kurchavov, M.L. Zheludkevich, G. Lefèvre, P. Volovitch, In situ surface film evolution during Mg aqueous corrosion in presence of selected carboxylates, Corros. Sci. (2020) 108484. In Press.

[44] J.D. Ramsey, R.L. McCreery, In situ Raman microscopy of chromate effects on corrosion pits in aluminum alloy, J. Electrochem. Soc. 146 (1999) 4076–4081.
[45] L. Xia, R.L. McCreery, Chemistry of a chromate conversion coating on aluminum alloy AA2024-T3 probed by vibrational spectroscopy, J. Electrochem. Soc. 145 (1998) 3083–3089.
[46] A. Abildina, A. Argimbayeva, A. Kurbatov, Y. Bakhytzhan, G. Rakhymbay, M. Wark, P. Bottke, Study of polarization characteristics of corrosion films on magnesium in sulfate-containing electrolytes, Appl. Sci. Basel (Basel) 10 (2020) 1406–1422.